Supporting file

Text S1

Characterization methods

X-ray diffraction (XRD) analysis was conducted using an X-Pert Powder Diffractmeter (Panalytical, Netherlands) with Cu K_α radiation (λ=0.15418 nm) at a rate of 0.02(°)/s. Raman spectroscopy was performed with a LabRAM Odyssey (HORIBA, France) in Raman shift range of 100−800 cm^{-1}. Fourier transform infrared spectroscopy (FT-IR) was taken using a VERTEX 80 (Bruker, Germany) in the wavelength range of 4000−400 cm^{-1}. Scanning electron microscope (SEM) images and energy-dispersive spectroscopy (EDS) mapping was acquired with a ΣIGMA–X–Max20 (ZEISS, German). UV-visible diffuse reflectance spectra (UV-Vis DRS) were recorded by a UV 2700 (Shimadzu, Japan), and the X-ray fluorescence spectroscopy (XRF) was conducted with an XRF–1800 (Shimadzu, Japan). Transmission electron microscope (TEM), high-resolution transmission electron microscope (HRTEM) images and energy dispersive X-ray spectroscopy (EDX) mapping were obtained with a Tecnai G2 F20 (FEI, USA). UV-visible diffuse reflectance spectra (UV-Vis DRS) were recorded by a UV 2700 (Shimadzu, Japan). Photoluminescence spectroscopy (PL spectra) were carried out using a FluoroMax–4 (HORIBA, France) with an excitation wavelength of 300 nm. X-ray photoelectron spectroscopy (XPS) was performed with a K−Alpha (Thermo Fisher Scientific, USA), a monochromatic Al source was used under a vacuum of 2×10^{-9} mbar with reference to C 1s peak (284.8 eV). Transient photocurrent response, electrochemical impedance spectroscopy (EIS) and Mott–Schottky plots were conducted on a CHI660C electrochemical workstation (Zhenhua, China). Electron spin resonance spectroscopy (ESR) was examined on EMXPLUS (Bruker, Germany) for DMPO–$\cdot O_2^-$ and DMPO–·OH. Zeta potentials were measured by a DelsaNano C (Beckman Coulter, USA). Action spectra of MB/TC photodegradation and H_2 evolution were tested via an RF–6000 fluorescence spectrophotometer (Shimadzu, Japan) in the range of 320−480 nm based on the UV-Vis DRS results and used Xenon lamp (Wavelength range: 320−780 nm). N_2 adsorption-desorption isotherms and pore distribution were measured with QuadraSorb SI (Boynton Beach, United States). Total organic carbon (TOC) in MB/TC photodegradation was measured by Shimadzu TOC-LCPH (Shimadzu, Japan).

Photocatalysis performance tests

The photocatalysis wastewater treatment activity was evaluated using the same self–build photo–chemical reactor. For the experiments, 80 mL MB (10 mg/L, pH=6.51 at 25 °C) or TC (20 mg/L, pH=1.61 at 25 °C) solution was used as simulated wastewater, and 20 mg catalysts were added into the reactor. Initially, the solution underwent a 30 min ultrasound treatment. This was followed by a 30-min dark adsorption phase; 5 mL solution was sampled every 30 min over the next 1 h under a light irradiation. The sampled solution was then centrifuged for 10 min, and the concentration was measured using a spectrophotometer at wavelengths of 664 nm for MB and 355.5 nm for TC. Error bars representing standard deviation (s.d.) were given in these tests. For study of the MB/TC fully degradation, a prolonged photodegradation was carried out for 6 h. The contaminant removal ratio (%) is calculated by the following formula (Eq. (S1)):

$$\text{Removal ratio}=(C_0-C_i)/C_0\times100\% \qquad \text{(S1)}$$

where C_0 and C_i is the initial and measured concentration of pollutant respectively.

Additionally, the photocatalytic water splitting for hydrogen (H_2) evolution was assessed using the same Xenon lamp as for organic degradation. This setup was equipped with a gas-closed photocatalytic circulation system (Labsolar–6A, PerfectLight, China), evacuation system, and an analysis system (gas chromatography with computer, GC9790 II, Fuli Instrument, China), as illustrated in Figure S1. The photocatalytic H_2 evolution experiments were conducted at 25 °C. Typically, 50 mg catalysts along with 5 mL MeOH (sacrificial agent [1]) and 30 mL of distilled water (pH of this MeOH solution is 6.91 at 25 °C) were treated via ultrasound for 10 min. The treated mixture was then transferred to the reactor. Before the reaction started, the mixture was degassed under vacuum to remove O_2 and other impurity gases. The gas experimental system was sampled every 30 min under continuous 3 h irradiation via circulation system, then the sample gas is delivered to analysis system and the H_2 yield is analyzed, meanwhile the data were recorded and collected synchronously via matched computer.

Error bars representing s.d. were given in H_2 evolution test. For study of the extended photocatalysis process, a prolonged photocatalytic H_2 evolution was carried out for 6 h.

Furthermore, for verifying the structure stability of synthesized photocatalysts after photocatalytic reactions, the structure stability test is carried out as following: collected the samples from the reaction solutions in photocatalytic MB/TC degradation or H_2 evolution experiments, followed by filtration these solutions, washing, collection, and drying for 12 h at 50 °C, then obtained the corresponding samples for different reaction system, which was named as CeO_2/TiO_2-MB for MB degradation, CeO_2/TiO_2-TC for TC degradation, and CeO_2/TiO_2-H_2 for H_2 evolution, respectively. Then the obtained samples were employed for XRD and SEM analyzing to evaluate the structure stability.

DFT simulation method

The combination mechanism on the rutile surface in CeO_2/rutile photocatalyst preparation was simulated via first-principles calculation based on DFT. Related to the XRD and HRTEM results, the rutile (110) plane was selected in this work. The calculations were performed using Cambridge Sequential Total Energy Package (CASTEP) module based on Materials Studio. For all calculations, crystal symmetry was not used. The rutile (110) matrix was constructed as shown in Figure S2(a) [2] under a supercell of 2×2×1. Ti_{6C} denotes the 6-coordinated Ti elements in the rutile, Ti_{5C} denotes the 5-coordinated Ti, O_{2C} denotes the 2-coordinated O, and O_{3C} means the 3-coordinated O. The electron exchange and correlation were treated within the Generalized Gradient Approximation (GGA) using the Perdew–Bruke–Ernzerh of (PBE) functional in all calculations [3], and DFT+U method was employed with U_{eff}=4.0 eV on Ti 3d states for rutile-based calculations [4]. The vacuum gap thickness was set to 15 Å. Gamma centered k-point meshes of 6×3×1 were used. The cut-off energy of the plane wave was 500 eV, and the energy convergence criterion was set as 10^{-4} eV. Adsorption energies (E_{ads}) were calculated using the formula (Eq. (S2)) [5]:

$$E_{\text{ads}}=E_{\text{total}}-(E_{\text{base}}+E_{\text{adsorbate}}) \quad \text{(S2)}$$

where E_{total} is the energy for the adsorption combined system, E_{base} is the energy of the used rutile base (as shown in Figures S2(a)–(c)), and $E_{\text{adsorbate}}$ is the energy of the adsorbate alone.

Meanwhile, Ti 3d and O 2p are proved to be CB and VB of rutile [6], and the photo-excited state was constructed via the photo-excited carrier generation and migration principle, achieved by adjusting the valence of Ti (+4 to +3) and O (−2 to −1) atoms on the surface layer in rutile (110) plane to simulate the exciting condition, where e^- on VB migrates to CB with h^+ generation on VB and photo-generated carriers will transfer to surface in photocatalytic reaction [7]. For evaluating the energy changes in the reactions, the energy change (ΔE) can be calculated as shown in Eq. (S3):

$$\Delta E=E_0-E_i \quad \text{(S3)}$$

where E_0 is the initial system energy and E_i is system energy in each reaction processes. Furthermore, oxygen vacancies play an essential role in adsorption [8], and the models for different oxygen vacancy were investigated and revealed in Figure S2(b) (with 1 O_{2C} vacancy, OV_{2C}) and Figure S2(c) (with 1 O_{3C} vacancy, OV_{3C}), respectively, while the oxygen vacancy formation energy (E_{FOV}) can be calculated as Eq. (S4) [9]:

$$E_{\text{FOV}}=E_{\text{OV}}-E_{\text{rutile}}+0.5E_{\text{oxygen}} \quad \text{(S4)}$$

where E_{OV} is the energy of the rutile with oxygen vacancy and E_{oxygen} is the energy of O_2.

In adsorption process study, the Ce^{3+} cations are chosen related to the $Ce(NO_3)_3$ solution in photocatalytic synthesis system, while Ce^{4+} is considered to represent CeO_2 as main reactive sites is Ce^{4+} ions of CeO_2 in CeO_2/rutile composite [10], so we choose Ce^{4+}–rutile (110) as simulated gained CeO_2/rutile compound instead. The most stable structure, Ce–rutile (110) as Figure S2(d) shown, is constructed as 1 Ce cation connected with 2 O_{2C} and 1 O_{3C} [11], and the Ce–rutile (110) with 1 OV_{2C} and 1OV_{3C} is built as Figures S2(e) and (f) shown separately [12].

Text S2

Apparent quantum yield (AQY) calculation details

All AQY calculations were processed with CeO_2/TiO_2-1:1. Based on the action spectra results (The highest quantum efficiency range at 340−430 nm), UV-Vis results (Absorption range is 200−450) and used Xenon lamp (Wavelength range: 320−780 nm), the calculated wavelength of light is set as λ=380 nm=380×10^{-9} m;

The calculated details for organic degradation are exhibited as Eq. (S5) [13]:

$$\mathrm{AQY} = \frac{\text{Number of degraded molecules}}{\text{Number of incident photon}} \times 100\% \tag{S5}$$

Energy of one photon (E_{photon}): $E_{\mathrm{photon}} = \frac{hc}{\chi} = \frac{6.6\times10^{-34}\times3\times10^{8}}{380\times10^{-9}} = 5.21\times10^{-19}\ \mathrm{J}$, h and c is Planck's constant and lightspeed separately;

The total energy of light falling (E_{total}): E_{total}=1 W/cm^2=10^4 W/m^2;

Number of photon: $\frac{E_{\mathrm{total}}}{E_{\mathrm{photon}}} = \frac{10^{4}\ \mathrm{W/m^2}}{5.21\times10^{-19}\ \mathrm{J}} = 1.92\times10^{22}$;

Number of MB (10 mg/L) molecules in 80 mL solution: $\frac{10\ \mathrm{mg/L}\times80\ \mathrm{mL}}{319.85\ \mathrm{g/mol}}\times N_{\mathrm{A}} = 1.51\times10^{18}$, N_{A} is Avogadro constant;

Number of TC (20 mg/L) molecules in 80 mL solution: $\frac{20\ \mathrm{mg/L}\times80\ \mathrm{mL}}{444.45\ \mathrm{g/mol}}\times N_{\mathrm{A}} = 2.16\times10^{18}$;

Area of exposed solution: πr^2=3.14×3=28.26 cm^2=0.002826 m^2;

Number of incident photon: 1.92×10^{22}×0.002826=5.43×10^{19};

Number of degraded molecules: Number of molecules×(Degradation ratio);

AQY of MB degradation: $\mathrm{AQY_{MB}} = \frac{1.51\times10^{18}\times95.83\%}{5.43\times10^{19}}\times100\% = 2.67\%$;

AQY of TC degradation: $\mathrm{AQY_{TC}} = \frac{2.16\times10^{18}\times72.84\%}{5.43\times10^{19}}\times100\% = 2.90\%$;

The calculated details for H_2 evolution are exhibited as Eq. (S6) [14, 15]:

$$\mathrm{AQY} = \frac{2\times\text{Number of evolved } \mathrm{H_2} \text{ molecules}}{\text{Number of incident photon}} \times 100\% \tag{S6}$$

Number of evolved H_2 molecules: H_2 production capacity × catalyst amount;

Area of exposed solution: πr^2=3.14×4^2=28.26 cm^2=0.005024 m^2;

Number of incident photon: 1.92×10^{22}×0.005024=9.65×10^{19};

AQY of H_2 evolution: $\mathrm{AQY}_{\mathrm{H_2\ evolution}} = \frac{2\times20\times10^{-3}\times29.19\times10^{-6}\times N_{\mathrm{A}}}{9.65\times10^{19}}\times100\% = 0.73\%$.

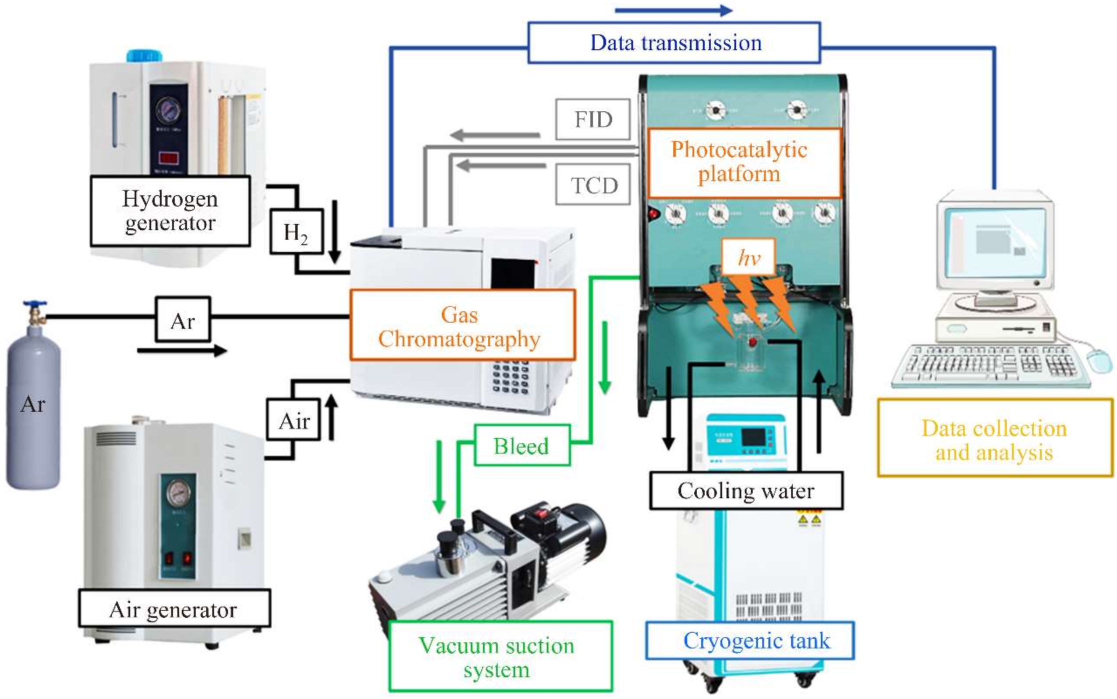

Figure S1 Sketch of the photocatalytic H_2 evolution reaction system

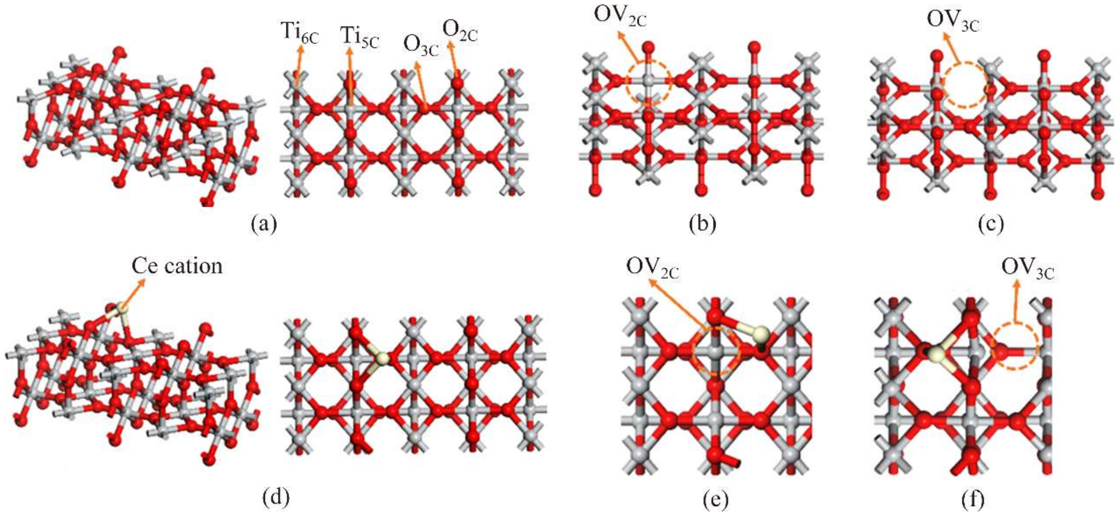

Figure S2 Structure schemes of (a) rutile (110) plane, rutile (110) with (b) 1 OV_{2C} and (c) 1 OV_{3C}, (d) Ce–rutile (110), Ce–rutile (110) with (e) 1 OV_{2C} and (f) 1 OV_{3C} (silver: Ti, red: O, yellow: Ce)

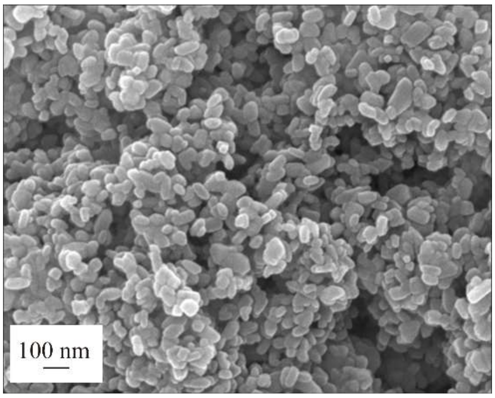

Figure S3 SEM image of rutile

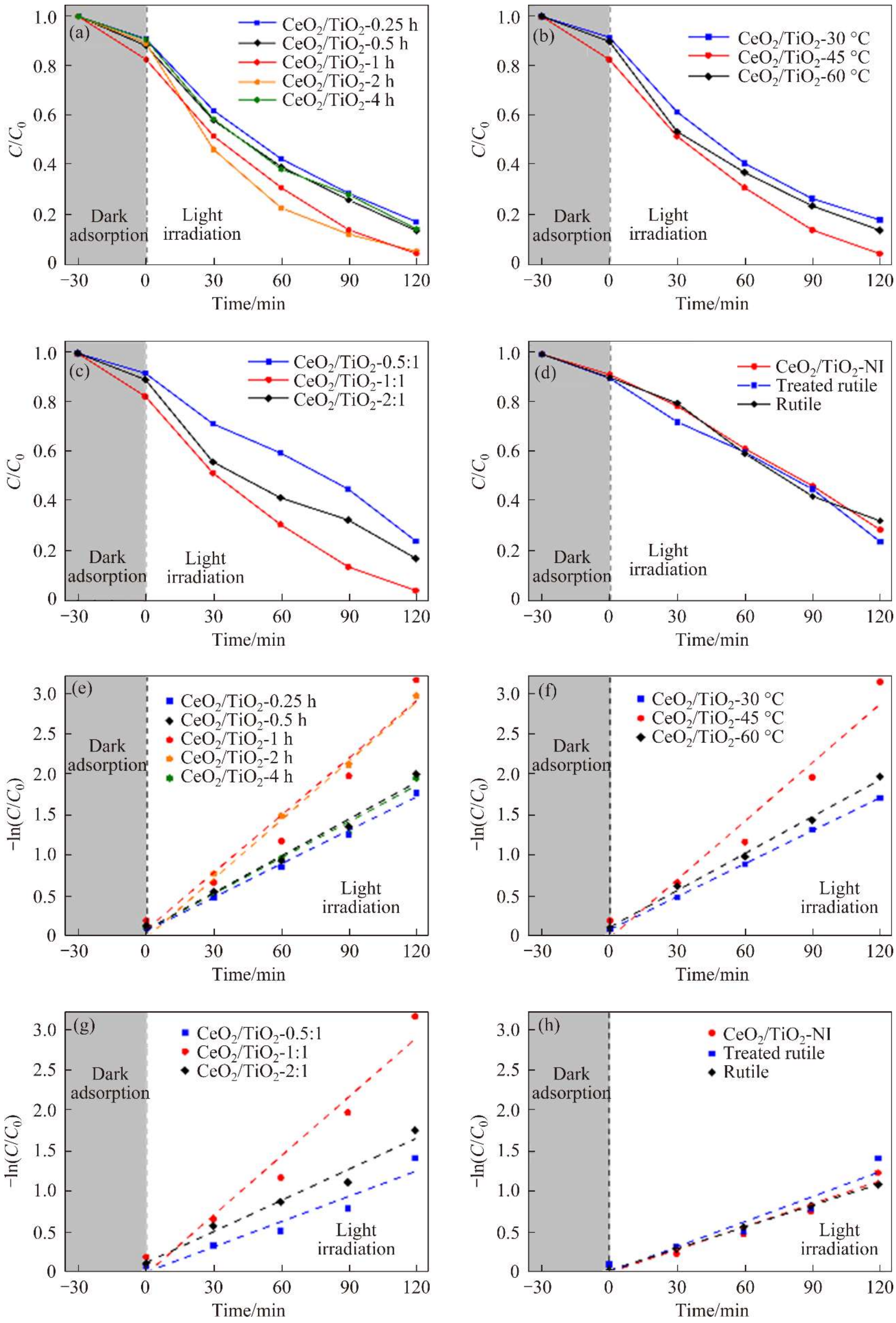

Figure S4 Photodegradation results for MB and the first-order kinetic fitting studies of samples synthesized with different conditions: (a, e) Irradiation time; (b, f) Water bath temperature; (c, g) $Ce(NO_3)_3 \cdot 6H_2O$: rutile molar ratio; (d, h) CeO_2/TiO_2-NI and treated rutile

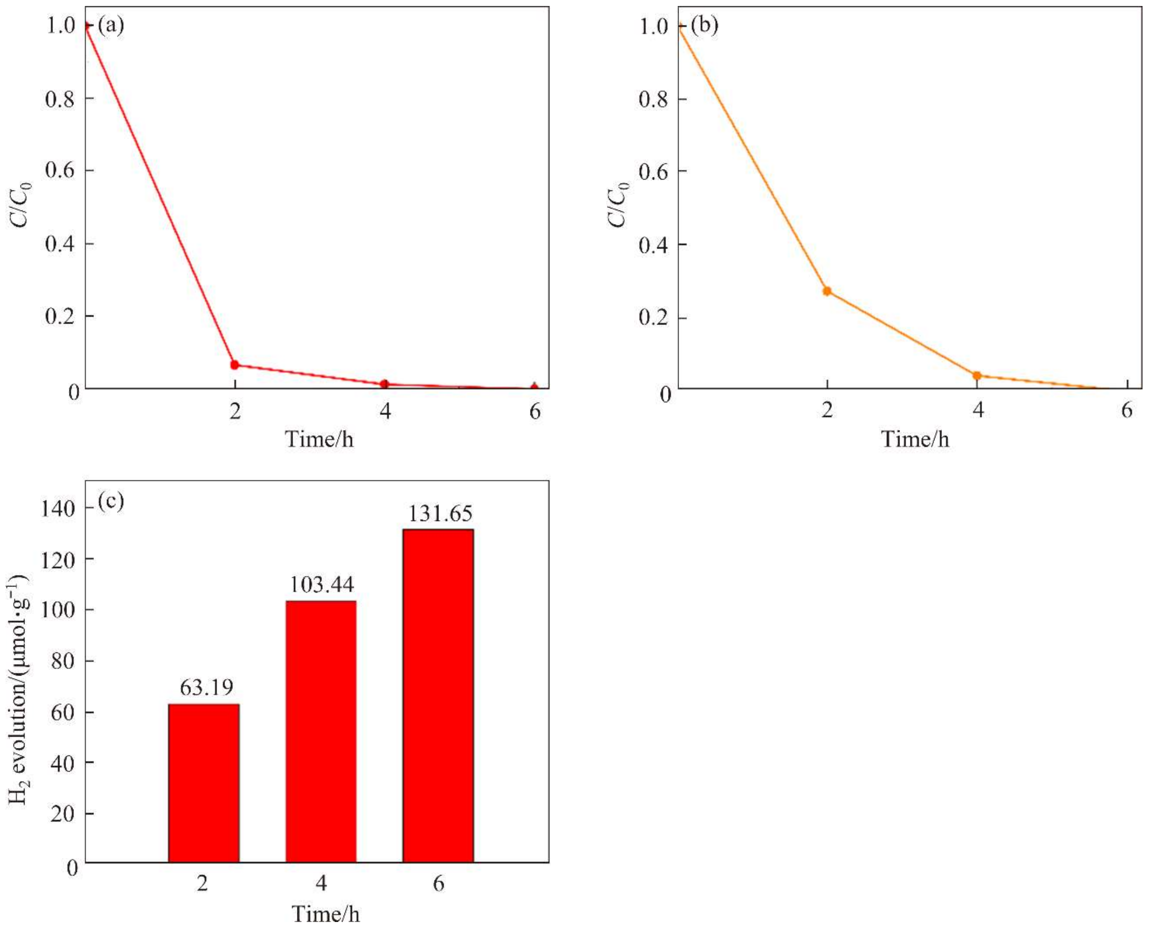

Figure S5 The long-term photocatalysis results (6 h) of (a) MB and (b) TC degradation, and (c) H_2 evolution of CeO_2/TiO_2-1:1

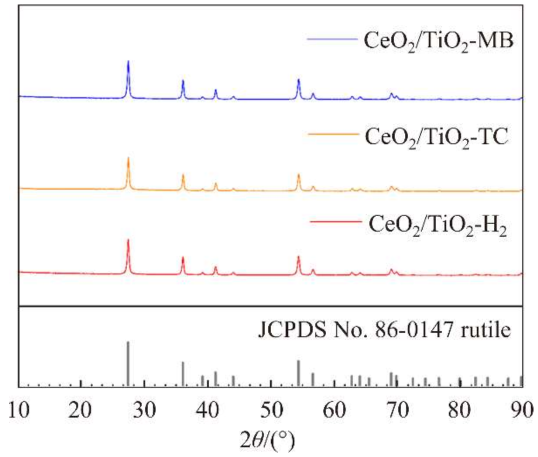

Figure S6 XRD patterns comparison among CeO_2/TiO_2-MB, CeO_2/TiO_2-TC and CeO_2/TiO_2-H_2

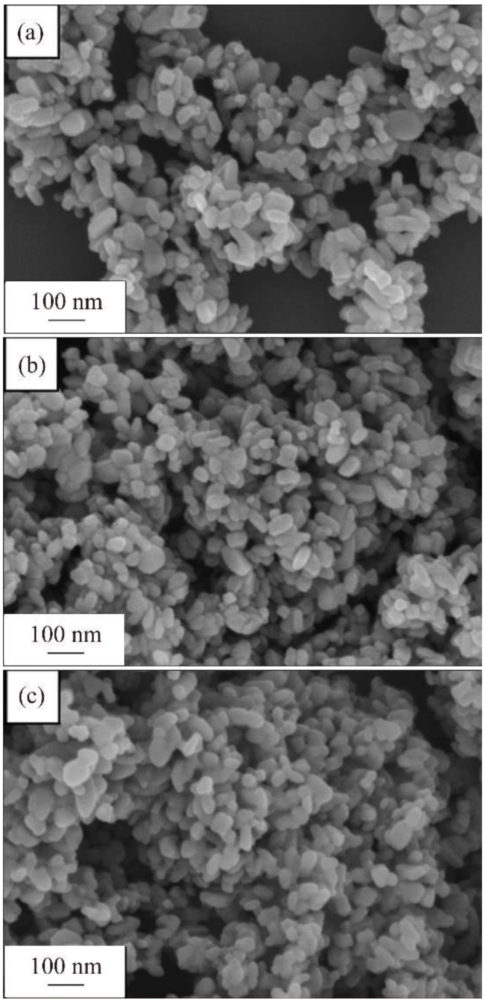

Figure S7 SEM images of (a) CeO_2/TiO_2-MB, (b) CeO_2/TiO_2-TC, and (c) CeO_2/TiO_2-H_2

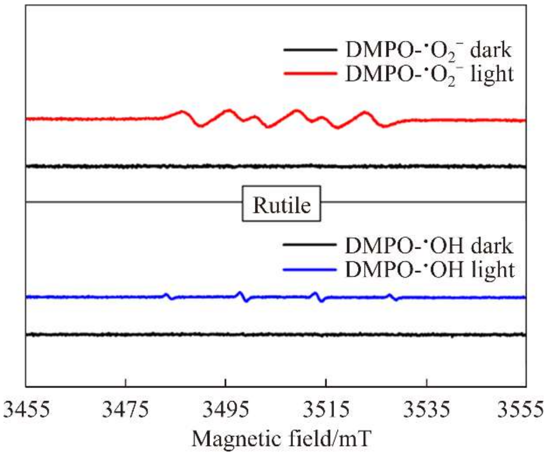

Figure S8 ESR spectra for DMPO–·O_2^- and DMPO–·OH of rutile

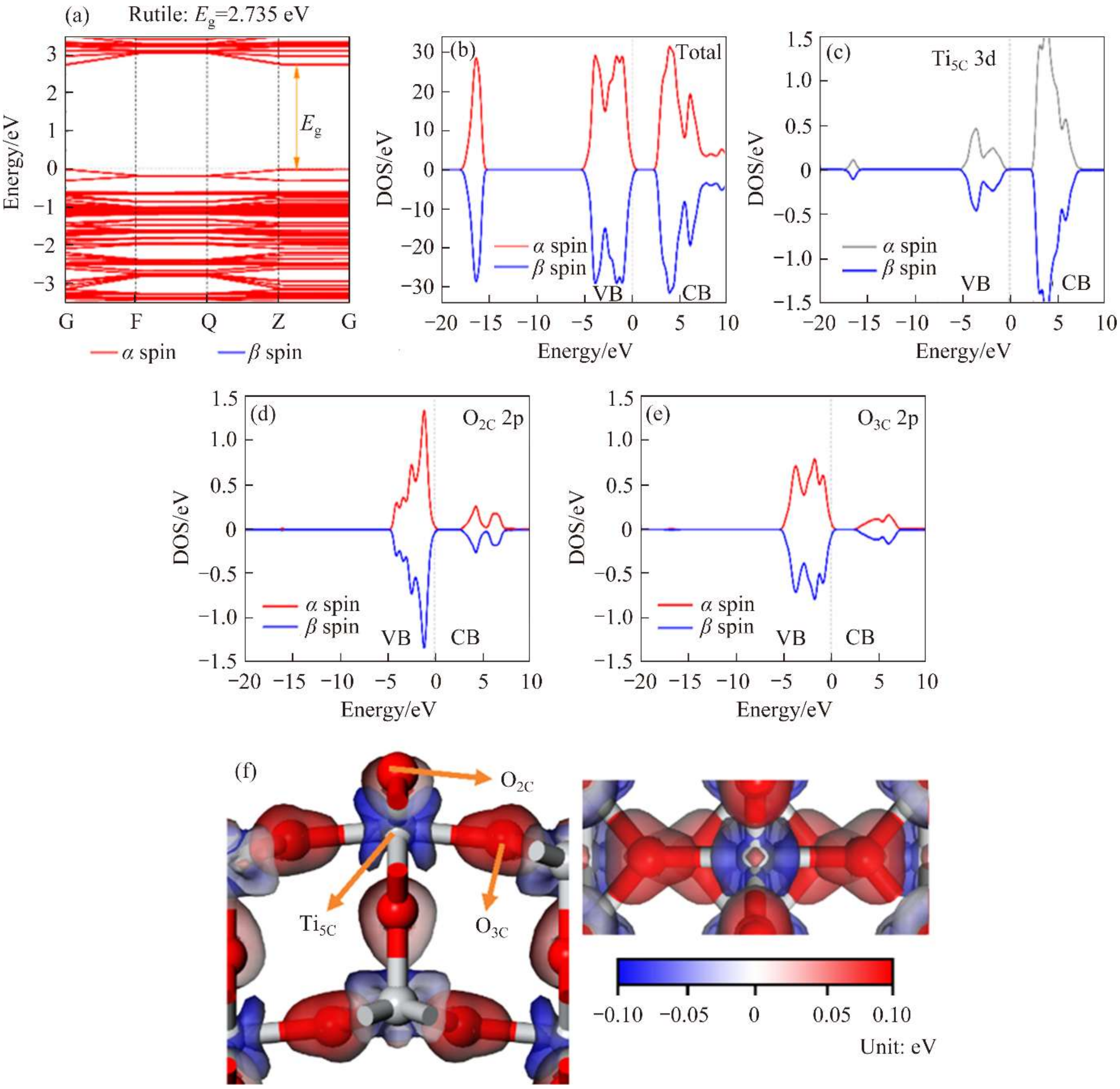

Figure S9 (a) Band structures, (b) TDOS, single atom PDOS of (c) Ti_{5C} 3d, (d) O_{2C} 2p and (e) O_{3C} 2p, and (f) DCD of rutile (110) facet

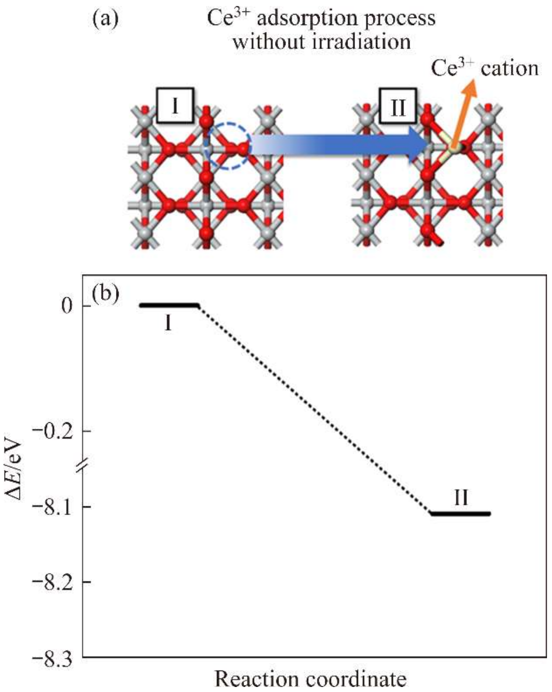

Figure S10 (a) Scheme and (b) reaction energy diagram of Ce^{3+} adsorption without irradiation

Table S1 Details of synthesis conditions

Sample	Illumination time/h	Water bath temperature/°C	Raw material molar ratio ($Ce(NO_3)_3\cdot6H_2O$: Rutile)
CeO_2/TiO_2-1:1 (1 h, 45 °C)	1	45	1:1
CeO_2/TiO_2-0.25 h	0.25	45	1:1
CeO_2/TiO_2-0.5 h	0.5	45	1:1
CeO_2/TiO_2-2 h	2	45	1:1
CeO_2/TiO_2-4 h	4	45	1:1
CeO_2/TiO_2 -30 °C	2	30	1:1
CeO_2/TiO_2 -60 °C	2	60	1:1
CeO_2/TiO_2-0.5:1	2	45	0.5:1
CeO_2/TiO_2-2:1	2	45	2:1
CeO_2/TiO_2-NI	—	45	2:1
Treated rutile	2	45	2:1
Rutile	—	—	—

Table S2 Average crystal sizes and lattice parameters of CeO_2/TiO_2-1:1 and rutile

Sample	Average crystal size/nm	Average lattice parameters/nm	
		a=*b*	*c*
CeO_2/TiO_2-1:1 (1 h, 45 °C)	26.5	0.459	0.296
Rutile	27.7	0.460	0.296

Table S3 MB removal ratios, *k* and R^2 of all synthesized samples

Sample	MB removal ratio/%	k/min^{-1}	R^2
CeO_2/TiO_2-1:1 (1 h, 45 °C)	95.83	0.025	0.94
CeO_2/TiO_2-0.25 h	83.00	0.014	0.99
CeO_2/TiO_2-0.5 h	86.56	0.015	0.99
CeO_2/TiO_2-2 h	94.89	0.024	0.95
CeO_2/TiO_2-4 h	85.87	0.015	0.98
CeO_2/TiO_2-30 °C	82.17	0.014	0.93
CeO_2/TiO_2-60 °C	86.38	0.015	0.98
CeO_2/TiO_2-0.5:1	75.85	0.010	0.94
CeO_2/TiO_2-2:1	82.85	0.013	0.95
CeO_2/TiO_2-NI	70.94	0.009	0.97
Treated rutile	75.76	0.01	0.96
Rutile	66.84	0.009	0.97

Table S4 TC removal ratios, *k* and R^2 of CeO_2/TiO_2-1:1 and rutile

Sample	TC removal ratio/%	k/min^{-1}	R^2
CeO_2/TiO_2-1:1 (1 h, 45 °C)	72.84	0.010	0.97
Rutile	40.65	0.004	0.98

Table S5 TOC removal results of CeO_2/TiO_2-1:1 for MB and TC photodegradation

Solution	TOC before degradation/(mg·L^{-1})	TOC after degradation/(mg·L^{-1})	TOC removal ratio/%
MB solution	28.31	10.26	63.76
TC solution	34.24	23.15	32.39

References

[1] GUZMAN F, CHUANG S S C, YANG Cheng. Role of methanol sacrificing reagent in the photocatalytic evolution of hydrogen [J]. Industrial & Engineering Chemistry Research, 2013, 52(1): 61−65.

[2] GRACIANI J, ORTEGA Y, FDEZ SANZ J. Carbon doping of the TiO_2 (110) rutile surface a theoretical study based on DFT [J]. Chemistry of Materials, 2009, 21(8): 1431−1438.

[3] PERDEW J, CHEVARY J, VOSKO S, et al. Atoms, molecules, solids, and surfaces: Applications of the generalized gradient approximation for exchange and correlation [J]. Physical Review B, Condensed Matter, 1992, 46(11): 6671−6687. DOI: 10.1103/physrevb.46.6671.

[4] CHENG Dao-jian, LAN Jian-hui, CAO Da-peng, et al. Adsorption and dissociation of ammonia on clean and metal-covered TiO_2 rutile (1 1 0) surfaces: A comparative DFT study [J]. Applied Catalysis B: Environmental, 2011, 106(3, 4): 510−519. DOI: 10.1016/j.apcatb.2011.06.010.

[5] ZHANG Min-hua, CHI Suo-cheng, HUANG He-yuan, et al. Mechanism insight into MnO for CO activation and O removal processes on Co(0001) surface: A DFT and kMC study [J]. Applied Surface Science, 2021, 567: 150854. DOI: 10.1016/j.apsusc.2021.150854.

[6] WEI Bao-huan, CALATAYUD M. The subsurface diffusion of hydrogen on rutile TiO_2 surfaces: A periodic DFT study [J]. Topics in Catalysis, 2022, 65(1): 270−280. DOI: 10.1007/s11244-021-01518-w.

[7] LIU Jia-fang, ZHANG Sheng-bo, WANG Wei-kang, et al. Photoelectrocatalytic principles for meaningfully studying photocatalyst properties and photocatalysis processes: From fundamental theory to environmental applications [J]. Journal of Energy Chemistry, 2023, 86: 84−117. DOI: 10.1016/j.jechem.2023.06.038.

[8] ZHANG Wen-hai, BIAN Zhao-yong, PENG Yi-yin, et al. Dual-function oxygen vacancy of BiOBr intensifies pollutant adsorption and molecular oxygen activation to remove tetracycline hydrochloride [J]. Chemical Engineering Journal, 2023, 451: 138731. DOI: 10.1016/j.cej.2022.138731.

[9] EMERY A A, WOLVERTON C. High-throughput DFT calculations of formation energy, stability and oxygen vacancy formation energy of ABO_3 perovskites [J]. Scientific Data, 2017, 4: 170153. DOI: 10.1038/sdata.2017.153.

[10] CHEN Jie, XIAO Yu-ting, WANG Nan, et al. Facile synthesis of a Z-scheme CeO_2/C_3N_4 heterojunction with enhanced charge transfer for CO_2 photoreduction [J]. Science China Materials, 2023, 66(8): 3165−3175. DOI: 10.1007/s40843-023-2443-0.

[11] LV Cun-qin, LIU Jian-hong, GUO Yong, et al. DFT + U investigation on the adsorption and initial decomposition of methylamine by a Pt single-atom catalyst supported on rutile (110) TiO_2 [J]. Applied Surface Science, 2016, 389: 411−418. DOI: 10.1016/j.apsusc.2016.07.111.

[12] HEYDARI H, ELAHIFARD M, BEHJATMANESH-ARDAKANI R. Role of oxygen vacancy in the adsorption and dissociation of the water molecule on the surfaces of pure and Ni-doped rutile (110): A periodic full-potential DFT study [J]. Surface Science, 2019, 679: 218−224. DOI: 10.1016/j.susc.2018.09.014.

[13] GHOSH S, CHAKRABORTY K, PAL T, et al. Photocatalytic degradation of tetracycline antibiotics by RGO-CdTe composite with enhanced apparent quantum efficiency [J]. Scientific Reports, 2023, 13: 19028. DOI: 10.1038/s41598-023-46120-0.

[14] ZHANG Qi-qi, CHEN Xin, YANG Zhong-shan, et al. Precisely tailoring nitrogen defects in carbon nitride for efficient photocatalytic overall water splitting [J]. ACS Applied Materials & Interfaces, 2022, 14(3): 3970−3979.

[15] CHIANG T H, LYU Hao, HISATOMI T, et al. Efficient photocatalytic water splitting using Al-doped $SrTiO_3$ coloaded with molybdenum oxide and rhodium–chromium oxide [J]. ACS Catalysis, 2018, 8(4): 2782−2788.